Dielectric Gratings Enhancing the Field of View in Low Dielectric Permittivity Elliptical Lenses

Campo, Marta Arias; Carluccio, Giorgio; Bruni, Simona; Llombart, Nuria

Important note
To cite this publication, please use the final published version (if applicable).
Please check the document version above.

Dielectric Gratings Enhancing the Field of View in Low Dielectric Permittivity Elliptical Lenses

Marta Arias Campo, *Graduate Student Member, IEEE*, Giorgio Carluccio, *Member, IEEE*,
Simona Bruni, and Nuria Llombart, *Fellow, IEEE*

Abstract— Low relative permittivity plastic elliptical lenses in combination with integrated focal plane arrays are a promising solution to be used in the future mm- and sub-mm wave systems. Their appeal lies in the availability of materials with moderate loss and light weight, and the possibility to use cost-effective manufacturing techniques. However, the achievable scanning angular range is relatively small with low permittivity lenses. In this contribution, we explore the use of dielectric gratings with modulated height integrated in the lens material, with the aim of enlarging the steering angle. The dielectric gratings synthesize a tilted feed pattern, reducing the reflection loss and spill-over when illuminating the lens off-focus. A quasi-analytic approach based on Floquet mode analysis of the gratings is used to synthesize the grating profile. This method is combined with an analysis in reception of the lens antenna. A wideband prototype in G-band (140–220GHz) has been fabricated, achieving a Field-of-View of $\pm25°$ with gain >30dB.

Index Terms—Beam steering, dielectric gratings, field of view (FoV), mm-wave, elliptical lens antenna, leaky-wave antenna, wideband communications.

I. INTRODUCTION

THE growing interest for mm- and sub-mm- waves in mass-market applications, such as communications and radar, demands the development of low-cost system and front-end concepts. In these higher frequencies bands, high-gain antennas are required to compensate for the higher path spreading loss and lower available output power. Plastic elliptical lenses with low relative dielectric permittivity, ε_r, represent attractive candidates to achieve the required high gain. This is due to their cost-effectiveness, light weight, and availability of materials with moderate loss. In [1], [2] linearly and circularly polarized elliptical lenses fabricated in plastic material ($\varepsilon_r{\sim}2.3$) reaching gains larger than 30dBi have been demonstrated. Thanks to the combination of low ε_r materials and LW feeds, aperture efficiencies larger than 75% were achieved over 40% bandwidth.

Despite the listed benefits of using low ε_r elliptical lenses, the low ε_r brings some penalty in terms of the beam steering

achieved when displacing the feed within the focal plane. The particular case of truncated elliptical lenses with high aperture efficiency (η_{ap}) for the broadside beam was studied in [1]. The lens steering capability enables the implementation of multi-beam planar Fly's eye elliptical lens arrays sharing a common ground plane. The planar configuration facilitates considerably the active front-end integration w.r.t. to other wide angle steering concepts with curved focal surfaces [3]–[5]. The high η_{ap} enables the realization of compact Fly's eye lens arrays. As discussed in [1], to reach high η_{ap} at broadside, a good compromise between the taper, spill-over and reflection efficiencies should be reached when placing the feed on the focus. However, this implies increasing spill-over and reflection losses when displacing the feed along the focal plane to perform beam steering. As a consequence the η_{ap} decreases, hindering compact lens sizes. The increase in the scan loss is higher for lenses with lower ε_r, as a larger off-focus displacement is needed to reach a certain scan angle (due to Snell's Law). The focus of this work will be to enhance the steering range in the low ε_r elliptical lens presented in [1], in order to profit from the rest of their listed advantageous properties.
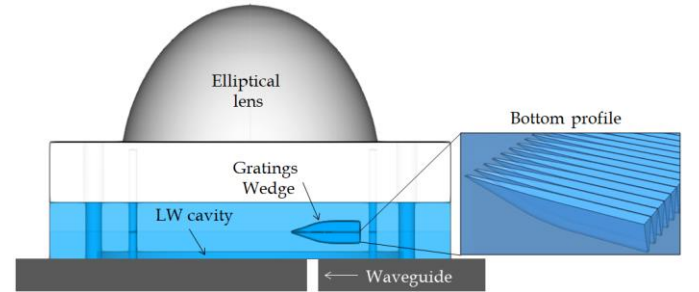

Fig. 1. Dielectric gratings with modulated height integrated in an elliptical lens. On the right, detail of one of the grating layers.

There are several concepts in the literature aiming to enlarge the field of view of integrated lenses with planar focal planes of feeds [6]–[13]. In [6] and [7] the design effort is focused on the lens or lens system shape, achieving very stable gain over the

Giorgio Carluccio is with NXP Semiconductors, High Tech Campus 46, 5656 AE, Eindhoven, The Netherlands.
Simona Bruni is with IMST GmbH, 47475 Kamp-Lintfort, Germany.
Nuria Llombart is with the THz Sensing Group, Delft University of Technology, 2628 CD Delft, The Netherlands.

scan angle. However, neither of them achieves high η_{ap} at broadside (~50%). In [7], the relative positioning between the objective and immersion lenses causes tolerance problems. In [8], the feed geometry is optimized to perform a beam-tilting in the radiation pattern inside the lens, improving the off-axis performance over a narrow band. References [9], [10] propose the combination of shaped lenses with an array of feeds in order to achieve maximum directivity at broadside and off-axis beams. However, the complexity of the array feeding network would be difficult to realize at high frequencies and would introduce high losses. Moreover, the design in [10] does not reach high η_{ap} at broadside (52%). In [11], the lens extension length is optimized in order to reduce the reflection loss. However, this implies losing 2.7dB in broadside directivity and increasing the side-lobe level. Other examples are based on 2D lenses, with enhanced scanning and high aperture efficiency in one plane [12], [13].

In this work, the use of dielectric gratings with modulated height, integrated inside a low ε_r elliptical lens, as shown in Fig. 1, is investigated. The aim is to enlarge the angular field of view achieved with the elliptical lens over a wideband, while maximizing η_{ap} over the whole scan range. This is achieved by introducing a wedge composed of dielectric gratings, on top of the wideband leaky-wave (LW) feed presented in [1]. The gratings with decreasing effective permittivity create a linear phase shift in the lens feed aperture field. This phase shift translates into a beam-tilt in the far-field, which reduces spill-over and reflection losses. Because the proposed grating wedge does not increase the LW feed directivity, the lens focal length is not modified. In [14], the introduction of a beam tilt in a horn antenna by means of metasurfaces was already proposed as a strategy to improve the performance of off-axis beams in reflectors. Dielectric gratings have been widely used in the literature to synthesize lenses [4], [5], [15]−[17], reflectarrays [18], polarizers [2], [19] or lens matching layers [20], [21]. The use of dielectric gratings as a mean of generating high directivity suffers from bandwidth or fabrication limitations, especially at high frequencies. In this work, we use the gratings instead to improve the steering performances of conventional elliptical lenses. This strategy allows us to reach high gains and large bandwidths. Additionally, the fabrication of the gratings with standard milling techniques is enabled at high frequencies.

The antenna architecture is shown in Fig. 1, where the dielectric gratings are also displayed. This pyramidal grating geometry in one dimension is based on the one used to build a polarizer in [2]. In this work we reuse this geometry, as it was proven to be suitable to be fabricated with standard milling techniques at frequencies higher than 100GHz. Pyramidal gratings present good transmission properties over the whole frequency band, preserving the wideband capability. The use of a resonant LW feed is a key enabler of this design. Thanks to its directive radiation pattern inside the lens, the gratings are not illuminated above their critical angle. Additionally, this relaxes the minimum required grating period to avoid grating lobes. The dielectric grating wedge (GW) is synthesized considering the incident field angles from the LW feed near-field. Those are calculated resorting to the multi-layer Spectral Green's Function. The grating transmission coefficients are computed applying a Floquet modes analysis, based on the Effective Medium Theory (EMT) [22]−[31]. The scan loss for each steered beam in the elliptical lens is minimized with an analysis in reception [1]. In this analysis, a reaction integral is performed on a surface defined inside the lens between the field radiated by the feed in transmission, and the incident field. The latter is associated to an oblique plane-wave with the targeted beam steering. The incident field is calculated inside the elliptical lens with the Geometrical Optics tool presented in [32].

A prototype in G-band has been fabricated and measured, showing $\pm 25°$ of beam steering with 3.6dB scan loss at the center frequency (180GHz). This represents 4dB improvement w.r.t. the case where the feed without GW is displaced along the focal plane [1]. This improvement is achieved over a wide band. A steering range of $\pm 25°$ would be sufficient to cover the elevation field of view in a football stadium small cell, as described in [33].

The paper is organized as follows: Section II describes the dielectric-grating wedge concept and geometry; Section III describes the GW synthesis methodology; Section IV describes the scan loss optimization with the analysis in reception; Section V presents the prototype fabrication and measurements validating the concept; Section VI provides some concluding remarks.

II. DIELECTRIC-GRATING WEDGE CONCEPT

In this section, the GW concept developed to enhance the FoV in elliptical lenses with low ε_r is discussed. The strategy followed in this work is to add a linear phase shift to the LW feed by using a non-periodic dielectric GW geometry integrated in the elliptical lens medium. The introduced linear phase shift, in turn, corresponds to a lateral displacement of the feed phase center. This enables a reduction of the spill-over and reflection losses for a certain steering angle.

The 1D pyramidal grating geometry which has been chosen is described as well in this section, analyzing its transmission properties in a periodic configuration. More in particular, the originated phase shift for different wave incident angles and polarizations is evaluated.

A. Leaky-Wave Feed with Dielectric Gratings Wedge

It is well known that by displacing the feed off-focus in integrated elliptical lenses, a beam steering is achieved in the lens radiation pattern [34]. The lateral feed displacement Δx required to achieve a beam steering angle ψ in a lens with focal distance F and dielectric permittivity ε_r, can be approximated as $\Delta x \approx F \sin \psi / \sqrt{\varepsilon_r}$ (Fig. 2a). For lenses with low ε_r, large displacements are required. Therefore, for a certain scan loss requirement, a small Field of View (FoV) is reached [34]. In [1], it was shown that for elliptical lenses with optimized truncation angles θ_{edge}, the FoV achieved with 3dB scan loss when displacing the feed along the focal plane is $\pm 15°$ with $\varepsilon_r = 2.3$. For $\varepsilon_r = 12$, it was shown that it reaches respectively $\pm 27°$ and $\pm 32°$ in the H- and E-planes.
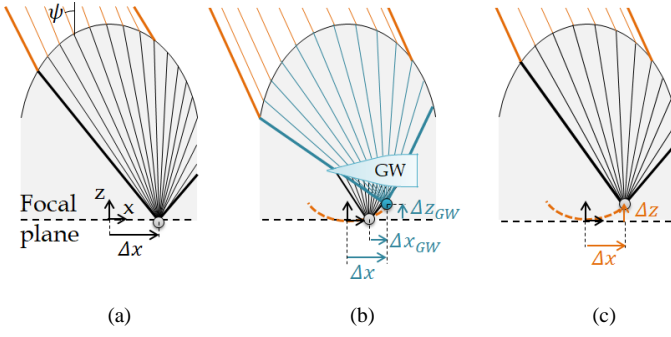
Fig. 2. Conceptual ray tracing representation of a) feed phase center displaced Δx along the elliptical lens focal plane, b) gratings wedge integrated in the elliptical lens, introducing a virtual phase center displacement $[\Delta x_{GW}, \Delta z_{GW}]$ with respect to the original feed, and c) feed phase center optimized laterally and axially.

The scope of this work is to enhance the steering capability of the elliptical lens with $\varepsilon_r = 2.3$, fed by the LW feed, presented in [1]. This LW or Fabry-Pérot feed consists on a half-wavelength air cavity between a ground plane and the lens [35], as shown in Fig. 1. Along the cavity, TE and TM LW modes propagate radially, generating a directive beam inside the lens. The LW is excited by a squared waveguide through a double-slot in the ground plane. For the broadside beam, this concept reaches 80% η_{ap} over 40% relative bandwidth. However, due to the low ε_r it presents a relatively small FoV ($\pm14°$ with 3dB scan loss). In order to enhance the beam steering capability in this elliptical lens, dielectric gratings in the same low ε_r material ($\varepsilon_r = 2.3$) are integrated on top of the LW feed, as shown in Fig. 1 and Fig. 2b. The gratings are designed to generate a linearly increasing phase shift in the LW feed field. This induces the desired phase center lateral displacement in the feed radiation pattern.

Similar pyramidal gratings were used in [2] to produce circular polarization. In that concept, the effective permittivity anisotropy in the gratings was exploited to generate 90° phase shift between two orthogonal linearly polarized waves. In this work, the height of the gratings is modulated, as shown in Fig. 3, leading to different effective permittivity. In contrast to the polarizer application, in this case the anisotropy axes are aligned with the field polarization, in order to avoid changes in the polarization. The use of this grating geometry is enabled by the fact that the LW feed radiates most of the energy below the critical angle between air and $\varepsilon_r = 2.3$. The low ε_r gratings provide wideband transmission coefficients [2]. This allows the feed input impedance to remain unchanged, enabling wideband steering enhancement.

By introducing a GW with varying height, leading to a linearly increasing phase shift, the initial feed phase center is displaced for the new system LW feed−GW in lateral and axial directions, as shown in Fig. 2b (Δx_{GW} and Δz_{GW}). Δx_{GW} is related to the linear phase shift introduced by the GW, and increases for larger phase variation; Δz_{GW} is caused by the lower effective permittivity of the GW with respect to the dielectric material, as already observed in [2]. The feed phase center (without gratings) should be originally placed on the coordinates $[\Delta x, \Delta z]$ to generate a beam pointing to ψ after the

elliptical lens (Fig. 2c). The optimum displacement ($\Delta x, \Delta z$) for different steering angles defines a curved surface which allows a reduction of the phase loss, as shown in [7]. This effect is similar to what happens in optical systems, where different steering angles lead to the definition of the Petzval surface [36]. Thanks to the phase center displacement originated by the gratings, the feed will be now placed at $[\Delta x - \Delta x_{GW}, \Delta z - \Delta z_{GW}]$ to generate the same steering angle after the elliptical lens. In this way spill-over and reflection loss are reduced, increasing the taper efficiency, as shown in Fig. 2b. The goal is therefore to maximize the linear phase shift slope generated by the gratings wedge (GW), in order to minimize the scan loss. The position of the new system LW feed−GW w.r.t. the lens focus ($\Delta x, \Delta z$) is optimized with the analysis in reception explained in Section IV. This analysis considers an oblique incident plane-wave with the desired impinging angle.
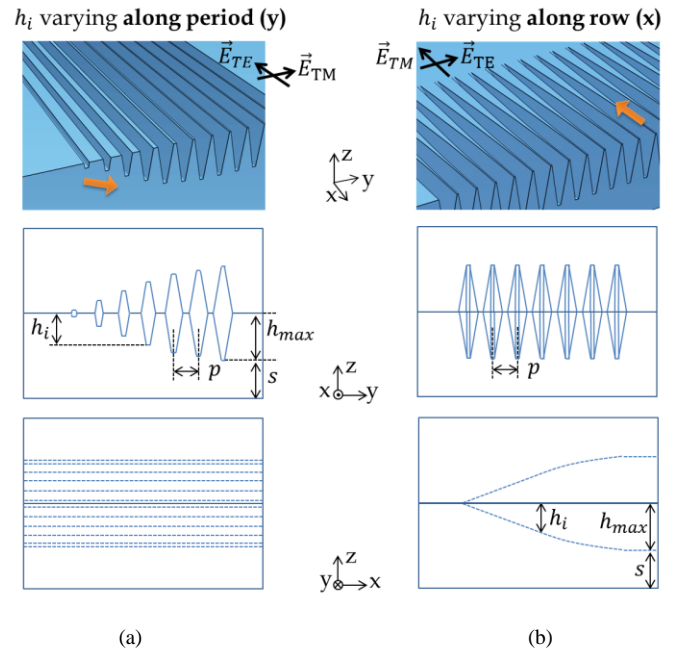

Fig. 3. Gratings fabrication with different heights. The maximum pyramid height ($h_{max} = 1.3$mm) is set by the period between gratings and the tool angle ($\alpha = 9.3°$). The pyramidal grating height varies along a) the period or b) each row. The steering takes place in the TM plane.

B. Gratings Geometry and Orientation

The gratings wedge is based on 1D double-sided pyramids, following the concept presented in [2]. The choice of this geometry is justified in Appendix I. The geometry of one pyramid is shown in the inset of Fig. 4b. The gratings slant angle is set by the standard milling tool slant angle [37]. The only variable is the grating height h, related to the tool penetration in the dielectric. The grating rows are milled at a periodic distance $p = 550$µm, avoiding grating lobes for incident angles up to 40° until 215GHz. For larger incidence angles the LW feed presents very low radiated power [1]. t_{bot} and α are set by the tool tip width and slant angle respectively. The maximum height achieved in the gratings for the chosen tool slant angle $\alpha = 9.3°$ is $h_{max} = 1.27$mm. This is set by the minimum $t_{top} = 30$um (Fig. 4b), to avoid breaking the grating

in the milling process. h_{max} determines the maximum phase shift that can be achieved with one layer of gratings.

The grating height variation can be performed along each row or along the period, as shown in Fig. 3. 1D gratings present anisotropic properties in their effective dielectric permittivity [22]. Therefore, depending on the grating orientation with respect to the field polarization, different phase shifts are reached for the same geometry. In order to perform a fast estimation of the transmission coefficients for a certain pyramid height, plane-wave incident angle, and field polarization, a Floquet mode model assuming local periodicity has been implemented. The model is based on a z-discretization of the pyramid in infinitesimal dielectric cubes, each of them modelled with EMT (EMT-FqW). The methodology, which takes into account the structure anisotropy, is discussed in Appendix II.
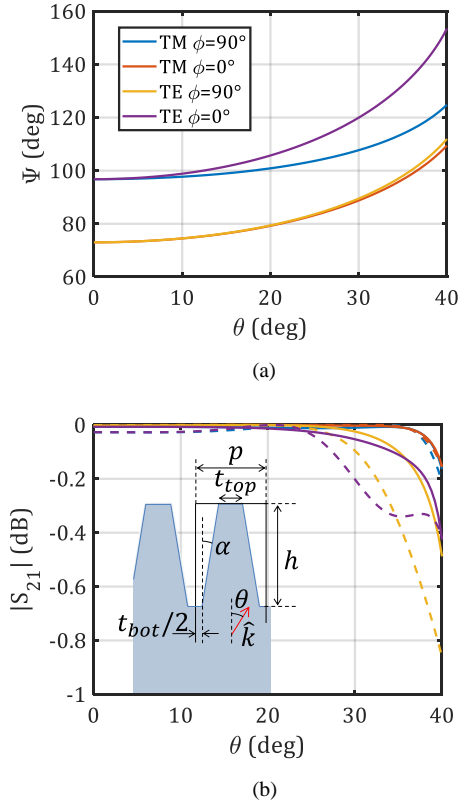

(a)

(b)

Fig. 4. a) Phase shift Ψ introduced by the pyramidal unit cell with $h = h_{max}$ w.r.t. a unit cell of the same height filled with dielectric, w.r.t. the angle in the dielectric θ and the azimuth steering angle ϕ, w.r.t. the reference system and field polarization in Fig. 3. b) Unit cell transmission coefficient amplitude ($|S_{21}|$) for the same polarization and ϕ steering planes as in a). Solid lines: single pyramid with $h = h_{max}$. Dashed lines: two pyramids with $h = h_{max}$ facing each other. Inset: Grating geometry, where $p = 550$um, $t_{bot} = 100$um, $\alpha = 9.3°$, and $t_{top} = p - t_{bot} - 2h \tan \alpha$.

The linear phase shift synthesized on top of the GW is evaluated as the phase difference between the phase of the field radiated by the LW in a homogeneous medium and the one of the LW in the presence of the grating geometry, at the same plane. Therefore the relevant design parameter is the phase shift Ψ, along the longitudinal component z, between a pyramidal unit cell with height h and a unit cell of the same height filled

with dielectric. This is calculated with respect to the incident angle θ in the homogeneous medium and the polarization as follows:

$$\Psi(\theta, h) = k_{zd}h - \Phi^{\text{TE/TM}}(\theta, h) \qquad (1)$$

where $k_{zd} = k_d \cos \theta$, k_d is the propagation constant in the dielectric and $\Phi^{\text{TE/TM}}$ is the phase of the scattering parameter $S_{21} = |S_{21}|e^{j\Phi}$ calculated by EMT-FqW for the evaluated grating, for the TE or TM mode. Assuming local periodicity and plane wave incidence, the phase shift associated to the transversal propagation component (k_ρ) cancels out and is therefore not present in (1), as it is derived from Snell's Law. The resulting phase shifts for different polarizations and cell orientations are plotted in Fig. 4a for $h = h_{max}$. The range of incident elevation angles where the LW feed radiates significant power is considered. This phase shift is the maximum that can be implemented in a single layer of gratings. The phase shift increases for larger elevation angles. On top of that, for scanning enhancement in the E-plane (TM mode), the favorable grating modulation plane to maximize the phase shift is $\phi = 90°$, whereas for the H-plane (TE mode) the optimum is $\phi = 0°$ (reference system in Fig. 3). Fig. 4b shows the unit cell transmission amplitude properties for the same cases considered in Fig. 4a. For $\theta > 40°$, the grating transmission coefficients degrade, due to the appearance of the critical angle and grating lobes. However, this does not represent a problem thanks to the LW feed, which radiates very low power for $\theta > 40°$ [1].

By using pairs of mirrored gratings, as displayed in Fig. 3, the transmission coefficients of the GW embedded in the elliptical lens are enhanced, as shown in Fig. 4b (dashed lines). In this way, the maximum synthesizable phase shift is at the same time doubled.

III. GRATING WEDGE SYNTHESIS

In this Section, the synthesis procedure to design the GW profiles is described. A GW with a pair of mirrored grating layers and $\phi = 0°$ orientation to enhance the steering in the H-plane is designed, as shown in Fig. 5b and Fig. 5c. The GW synthesis is performed iteratively using an approximated ray tracing via the application of the implemented EMT-FqW model for the gratings (Appendix II). First, the requirements in terms of phase shift to be introduced by the GW are derived. Next, the steps to design the GW profile, to reach the given phase profile at its top, are clarified, together with the taken approximations in the ray tracing procedure. Finally, the synthesis and results are shown, comparing the achieved phase profile in a full-wave (FW) simulation with the required one.

A. Phase Shift Requirement for Gratings Wedge

The linear phase shift requirement on top of the GW, Ψ_t, is defined at $z_t = 4.54$mm (Fig. 5b) within $x = \pm 3.34$mm. Here, the LW near-field amplitude edge taper is -8dB at z_t (Fig. 6a). The chosen amplitude taper results in a good compromise between maximizing the synthesized phase slope, and preserving the near-field amplitude after the GW. This will be discussed in Section IV. The coordinates z_b, z_c, and z_t in Fig.

5b are known, assuming that each grating layer will reach the height h_{max} at its edge, and considering that the grating should be supported by a dielectric layer of at least 1mm thickness, due to fabrication restrictions (s in Fig. 3 and Fig. 5b). Let's define Ψ_t as the linear phase associated to a θ_{FF} steering angle in the feed far-field inside the lens as

$$\Psi_t(x) = k_d x \sin \theta_{FF} \qquad (2)$$

(a)

The GW, which is thick in terms of wavelength ($2h_{max} > 2\lambda_d$, being λ_d the wavelength in the dielectric), is divided in two mirrored layers. Each layer will be assigned with half of the required phase shift. Thus the requirement defined at z_t, Ψ_t, is propagated backwards to z_c and divided by two, in order to synthesize the mirrored profiles. The backward propagation is performed with an approximated ray tracing. For this, the wave propagation direction in the homogeneous medium of the LW without gratings is used, as shown in Fig. 7a. The mapped phase requirement at z_c, Ψ_c, is calculated as

$$\Psi_c(x) = \Psi_t\big(x \pm \Delta x_0(x)\big)/2 \qquad (3)$$

for $x \gtrless 0$, where $\Delta x_0(x) = h_{max} \tan \theta_t(x)$, being θ_t calculated from the LW feed wave propagation vector at $z = z_t$, $\hat{k}_t$.

The wave propagation angles for the requirement mapping, as well as later on for the lens synthesis, are approximated by using the Poynting vector direction of the LW feed near-field without lens (Fig. 6b). This is calculated as $\theta = \cos^{-1}(\hat{z} \cdot \hat{k})$, where $\hat{k} = \vec{S}/|\vec{S}|$ with $\vec{S} = \frac{1}{2}Re\{\vec{E} \times \vec{H}^*\}$, being $\vec{E}$ and $\vec{H}$ the LW feed electric and magnetic near-fields. The LW feed near-fields are calculated integrating the corresponding SGF and current distribution of the LW feed [1]. The far-field approximation gives already relatively good results for the field amplitude taper at z_b, z_c, and z_t as shown in Fig. 6a. However, the near-field propagation direction is more accurate at the grating edges, as shown in Fig. 6b.
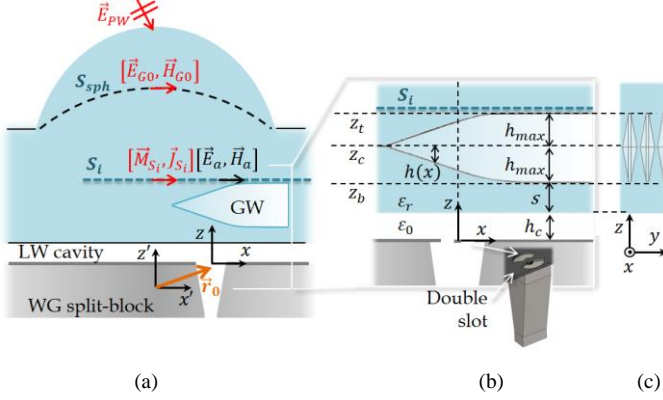
Fig. 5. a) Antenna geometry, fields and currents used for the analysis in reception. The coordinate system (x', z') is centered in the ellipse focus; (x, z) is centered in the double-slot feed. b) 2D drawing of the synthesized gratings wedge. The gratings height varies along each row, as shown in Fig. 3b. The blue area represents the dielectric, the shaded area the pyramids and the white area the air. $h_c = 940$um, $h_{max} = 1.27$mm, $s = 1$mm, $z_t = 4.54$mm, S_i at $z = 4.7$mm. c) Side view of the gratings, showing the pairs of mirrored pyramids to reduce reflection.
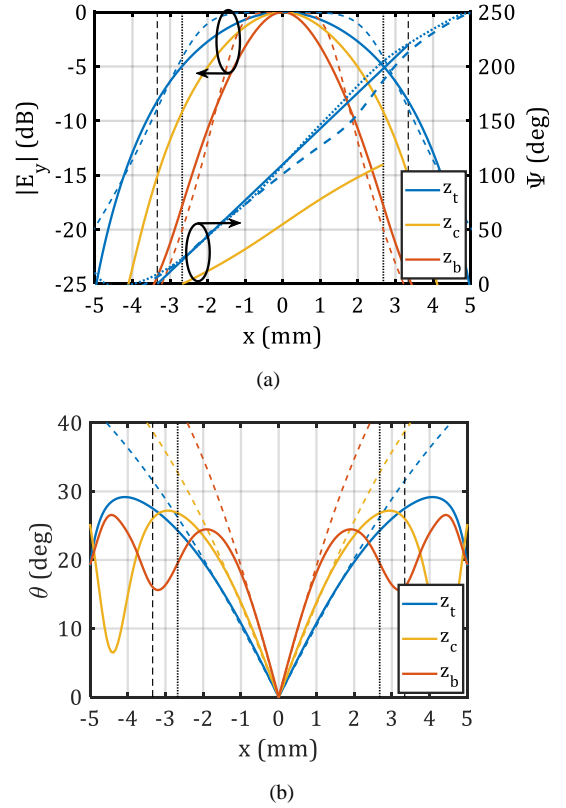

(b)

Fig. 6. a) Left axis: LW feed field amplitude (without GW) in the H-plane at 180GHz at the z coordinates marked in Fig. 5b. Solid line: near-field calculation. Dashed line: far-field calculation projected in the z-planes. Right axis: phase shift w.r.t. the LW without GW. Solid: requirements Ψ_t (blue line) and Ψ_c (yellow line). Dashed: FW simulations with the first calculated profile, h_0. Dotted: FW simulations with the final calculated profile, h. b) Poynting vector direction for the field and planes shown in a). Solid: calculated from the near-fields. Dashed: geometric approximation ($\theta = \tan^{-1}\left(\frac{x}{z-\Delta z}\right)$), being $\Delta z = -950$µm the far-field phase center displacement in z w.r.t. the LW ground plane. In both plots, vertical dashed lines mark the limits within Ψ_t is defined, and vertical dotted lines where Ψ_c is defined.

In order to approximately estimate the maximum phase shift that can be obtained at the edge of the GW, the incident angles of the field that impinges each layer at the maximum x_n should be considered. The first profile iteration is calculated with the phase requirement defined at z_c, Ψ_c. Therefore, the $x-$boundaries calculated with the approximate ray tracing, within Ψ_c is defined, will be taken as reference (marked in Fig. 6 with vertical dotted lines). In Fig. 6b, it can be seen that, at these boundaries, the incident angle stays below 25° and 30° in z_b, z_c, and z_t. Considering these incident angles, and the phase shift reached with a grating with h_{max} (Fig. 4a), it can be concluded that a maximum phase shift of 110°−120° can be achieved per grating layer. For the two layers, we finally set a linearly increasing phase shift requirement Ψ_t from 0° to 220° at z_t (Fig. 6a). This corresponds to a tilt in the feed radiation pattern inside the lens of approximately $\theta_{FF} = 5.7°$ at 180GHz (2). Fig. 6a shows the phase shift requirements at z_t and z_c.

The maximum phase shift achieved on both grating layers determines the maximum scan range achieved in the elliptical
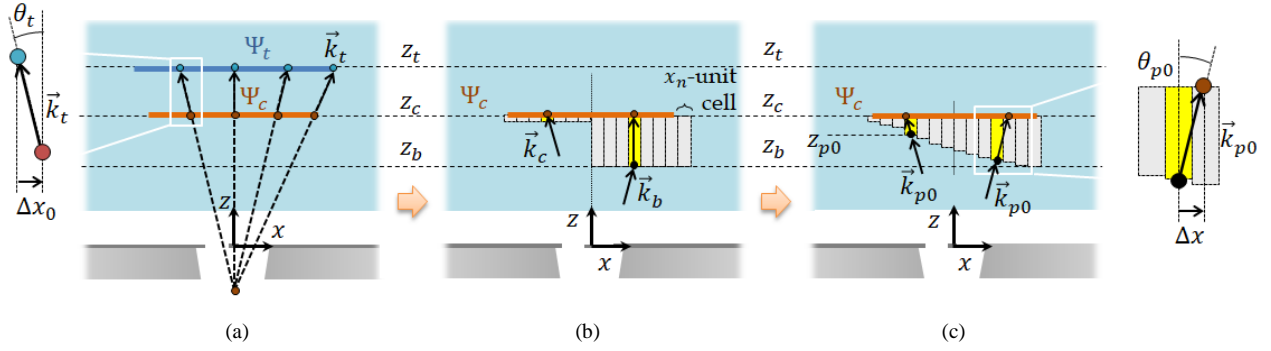
Fig. 7. a) Phase requirement at GW top and center z-planes. b) Unit cell mapping and incident angles for GW profile synthesis in first iteration, c) Unit cell mapping and incident angles in second iteration.

lens. If a higher phase shift could be reached with the gratings, θ_{FF} would be larger. Consequently, the scan loss at larger steering angles would decrease. The generation of larger phase shifts may be possible with, e.g., gratings with higher dielectric permittivity or with vertical walls (rectangular, cylindrical perforations). However the fabrication will be more difficult at these high frequencies (see Appendix I).

B. Synthesis of Grating Wedge Profile

In the following, we describe the synthesis process for the grating layer pair forming the GW (Fig. 5b). As explained in the previous section, the phase shift requirement has been defined at z_c, where the GW is centered, as Ψ_c (Fig. 7a). The GW is discretized in unit cells with x-coordinates x_n, representing two mirrored pyramids (Fig. 5c). The mirrored unit cells have unknown height $h(x_n)$, being h_{max} the maximum achievable height (Fig. 5b). The grating height $h(x_n)$ can be determined applying the EMT-FqW model discussed in Appendix II. The input parameters are the wave incident angle, polarization, and required phase shift in each unit cell. The implementation of the EMT-FqW model enables a fast calculation of $h(x_n)$, known the mentioned input parameters. Alternatively, a table with the phase shift obtained with all possible combinations among these three input parameters could be created with FW Floquet mode simulations. Nevertheless, this solution would be more time consuming.

The assignment of the phase shift requirement to a certain unit cell and the unit cell height calculation cannot be decoupled, as they are related by the gratings geometry itself. The definition of a grating profile equation to find this relationship is not a trivial task, for several reasons: 1) the propagation angle inside the pyramid changes with z and does not have a closed form (see Appendix II); 2) when considering unit cells with infinitesimal width, each ray crosses laterally unit cells with different heights, which should be considered in form of a graded effective permittivity in x direction; 3) the incident wave has a spherical phase front, and consequently different incident angles along x direction should be taken into account. In other works reported in the literature, the analysis is simplified as the effective permittivity changes only laterally in the gratings [17], and not also axially as in this work.

In this work, a simplified iterative approach is proposed to derive the gratings profile. This procedure reaches sufficient accuracy in the synthesized phase shift feature with two iterations. The lateral wave propagation cannot be neglected due to the grating significant and variable thickness (up to ~$0.75\lambda_0$ per layer) and the wide incident angles associated to the LW feed (up to 30°). Therefore, already in the first iteration, displayed in Fig. 7b, the lateral propagation is taken into account by evaluating the phase requirement at the center of the layer pair, z_c in Fig. 5b.

The phase shift requirements are assigned to each x_n-unit cell as shown in Fig. 7b. The pyramid height h_0 at each x_n is then approximated solving

$$\Psi_c(x_n) = k_d \cos[\theta(x_n)] h_0(x_n) - \Phi^{TE}[\theta(x_n), h_0(x_n)] \quad (4)$$

where k_d is the propagation constant in the dielectric, $\theta(x_n)$ is the propagation angle in the dielectric considered for the x_n-unit cell and $\Phi^{TE}(\theta, h_0)$ is the phase evaluated with the equivalent EMT-FqW model at z_c.

The incident angle should be evaluated along the gratings profile, but this is still unknown. Hence, in the first step, we assume that the GW starts with $h = 0$ on the left side, and will reach h_{max} on the right side. We therefore divide the grating profile in two regions:

For $x_n < 0$, it is assumed that the gratings will have a small height, as the required phase difference is small in this region. Therefore, a good approximation for the incident angle on the unknown grating surface, $h(x_n, z_n)$, is the one dictated by the LW feed Poynting vector at z_c ($\hat{k}_c(x_n)$ in Fig. 7b).

For $x_n > 0$, it is assumed that the gratings will have a large height, to create large phase shifts. A good approximation for the incident angle on the unknown grating surface, $h(x_n, z_n)$, is the one dictated by the LW feed Poynting vector at $z_b = z_c - h_{max}$ ($\hat{k}_b(x_n)$ in Fig. 7b).

Assuming these incident angles, resorting to eq. (4), we estimate the first approximation for the profile, h_0, shown in Fig. 8. Once a first approximation for the profile is known, $z_{p0}(x_n) = z_c - h_0(x_n)$, a refinement with a second iteration is performed. This time, the incident angle and phase requirement can be evaluated along the GW bottom profile calculated in the first iteration, z_{p0}, as shown in Fig. 7c. In this way, the final grating profile h is synthesized solving

$$\Psi_c[x_n \pm \Delta x(x_n)] =$$

$$k_d \cos\theta_{p0}(x_n)\, h(x_n) - \Phi^{TE}\big[\theta_{p0}(x_n), h(x_n)\big] \qquad (5)$$

for $x \gtrless 0$, where $\Delta x(x_n) = h_0(x_n)\tan[\theta_{p0}(x_n)]$, and θ_{p0} is calculated from $\hat{k}_{p0}$ (Fig. 7d). By approximating the propagation vector inside the gratings by the propagation vector $\hat{k}_{p0}$ in the dielectric (denser medium), an error is introduced in the calculated Δx. The maximum error can be evaluated comparing Δx estimated with $\hat{k}_{p0}$ in the dielectric, with the transmitted angle in a unit cell with the lowest effective permittivity, $\varepsilon_{eff} \sim 1.4$ (for $h_i = h_{max}$). Taking into account the maximum angle in the dielectric, $\theta_{p0} \sim 30°$, the transmitted angle for $\varepsilon_{eff} \sim 1.4$ is $38°$. As a result, the committed error in the estimated Δx is $270\mu m$ ($< \lambda_d/4$).

The initial and final calculated layer profiles are shown in Fig. 8. As shown as well in Fig. 5b, for $x > 0$ the lens is extended further with dummy gratings with maximum height until the field taper reaches -20dB at z_t (5.5mm) at the center frequency. This avoids an abrupt change in the boundary conditions, which would degrade the grating transmission properties. For the same reason, in y-direction, the gratings are periodically repeated to cover the area with a field taper larger than -20dB (± 5.2mm).

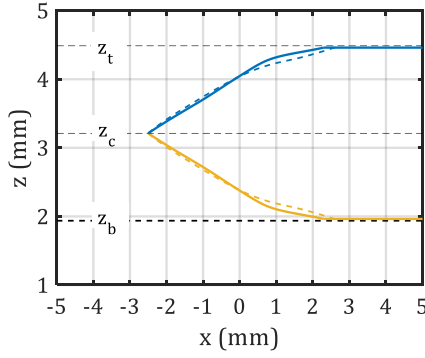Fig. 8.   Initial, h_0, (dashed line) and final, h, (solid line) lens profiles.

C. Full-Wave Simulation Results

The synthesized GW in the presence of the LW feed has been FW simulated with EMPIRE XPU [38]. The FW simulations include the effects of multiple reflections in the GW. The phase difference obtained between the LW near-fields without and with gratings at S_i, $z = 4.7$mm, is shown in Fig. 6a, in good agreement with the defined Ψ_t. For the profile calculated in the first iteration, h_0, the maximum error in the synthesized phase shift is $20°$, whereas for the profile calculated in the second iteration, h, the error is reduced to $7°$. The impact of this accuracy in the scan loss of the elliptical lens will be evaluated in Section IV.

The LW near-field amplitude and phase without and with GW at S_i are shown respectively in Fig. 9a and Fig. 9b, with the reference system in Fig. 5. The results correspond to the profile calculated in the second iteration. It can be seen that the near-field amplitude changes after the GW with respect to the LW field radiating in a homogeneous medium. This effect is related

to the tilt in the field propagation, associated to the synthesized linear phase, which is already visible after the GW (Fig. 9b on the right). The obtained amplitude effect is positive in terms of the lens scan loss, as it will be discussed in Section IV. The near-field obtained at S_i after the GW in the FW simulations is used in the analysis in reception discussed in Section IV. The goal of this analysis is to minimize the scan loss for a certain beam steering direction.

IV. SCAN LOSS OPTIMIZATION: ANALYSIS IN RECEPTION

In order to maximize the elliptical lens η_{ap} for a beam steering to a certain angle, an analysis in reception of the full antenna system (LW feed, GW, and elliptical lens) is proposed, as in [1]. The optimization parameter is the displacement vector $\vec{r}_0$ of the LW feed−GW system inside the elliptical lens, with respect to its focus (Fig. 5a).

The η_{ap} can be calculated dividing the power P_L delivered to the matched load connected to the feed in reception operative mode, by the power P_{in}^{rx} from a plane wave $\vec{E}_{PW}$ with a certain oblique incident direction, $\vec{k}_i$, as discussed in [1]

$$\eta_{ap} = \frac{P_L}{P_{in}^{rx}} = \frac{|V_{oc}I_{tx}|^2}{16 P_{rad}^{tx} P_{in}^{rx}} \qquad (6)$$

where $P_{in}^{rx} = 1/(2\zeta_0)\,|\vec{E}_{PW}|^2 A_{lens}$, being A_{lens} the projected lens area, and P_{rad}^{tx} is the power radiated by the feed calculated in an infinite medium and excited by the current I_{tx}. $|V_{oc}I_{tx}|$ can be calculated by performing a reaction integral over a spherical surface inside the elliptical lens centered on the focus, S_{sph} in Fig. 5a, between 1) the Geometrical Optics field, $[\vec{E}_{GO}, \vec{H}_{GO}]$, generated by a plane wave incident onto the lens, and 2) the fields radiated by the lens feed in an infinite medium, $[\vec{E}_a, \vec{H}_a]$. In order to optimize the scanning performance in a certain direction, the fields $[\vec{E}_{GO}, \vec{H}_{GO}]$ are evaluated at S_{sph} using the tool in [32]. This considers a plane wave incident from the targeted direction. Since the proposed grating is electrically thick, one cannot use a far field approximation to evaluate the fields $[\vec{E}_a, \vec{H}_a]$ in S_{sph}. It is therefore more convenient to evaluate the reaction integral directly over S_i (instead of S_{sph}) as follows [1]:

$$V_{oc}I_{tx} = \iint_{S_i}\big(\vec{H}_a \cdot \vec{M}_{S_i} - \vec{E}_a \cdot \vec{J}_{S_i}\big)dS \qquad (7)$$

where $[\vec{E}_a, \vec{H}_a]$ are the feed near-fields at S_i including the GW, estimated with FW simulations including multiple reflections (Fig. 9), and $[\vec{M}_{S_i}, \vec{J}_{S_i}]$ are the equivalent currents induced at S_i by the fields $[\vec{E}_{GO}, \vec{H}_{GO}]$ for the specific analyzed plane wave direction. The fields at S_{sph}, $[\vec{E}_{GO}, \vec{H}_{GO}]$, are propagated inside the lens and calculated at S_i. The incident fields at S_i, $[\vec{E}_i, \vec{H}_i]$, are obtained with the Green's Function for homogeneous media. The induced currents at S_i can be calculated as $\vec{J}_{S_i} = \hat{n} \times \vec{H}_i$ and $\vec{M}_{S_i} = -\hat{n} \times \vec{E}_i$ where $\hat{n}$ is the normal to the surface S_i, in our case $\hat{n} = \hat{z}$.

The reaction integral in (7), and therefore η_{ap}, is maximized when the conjugate of $[\vec{E}_a, \vec{H}_a]$ is equal to $[\vec{E}_i, \vec{H}_i]$. For a
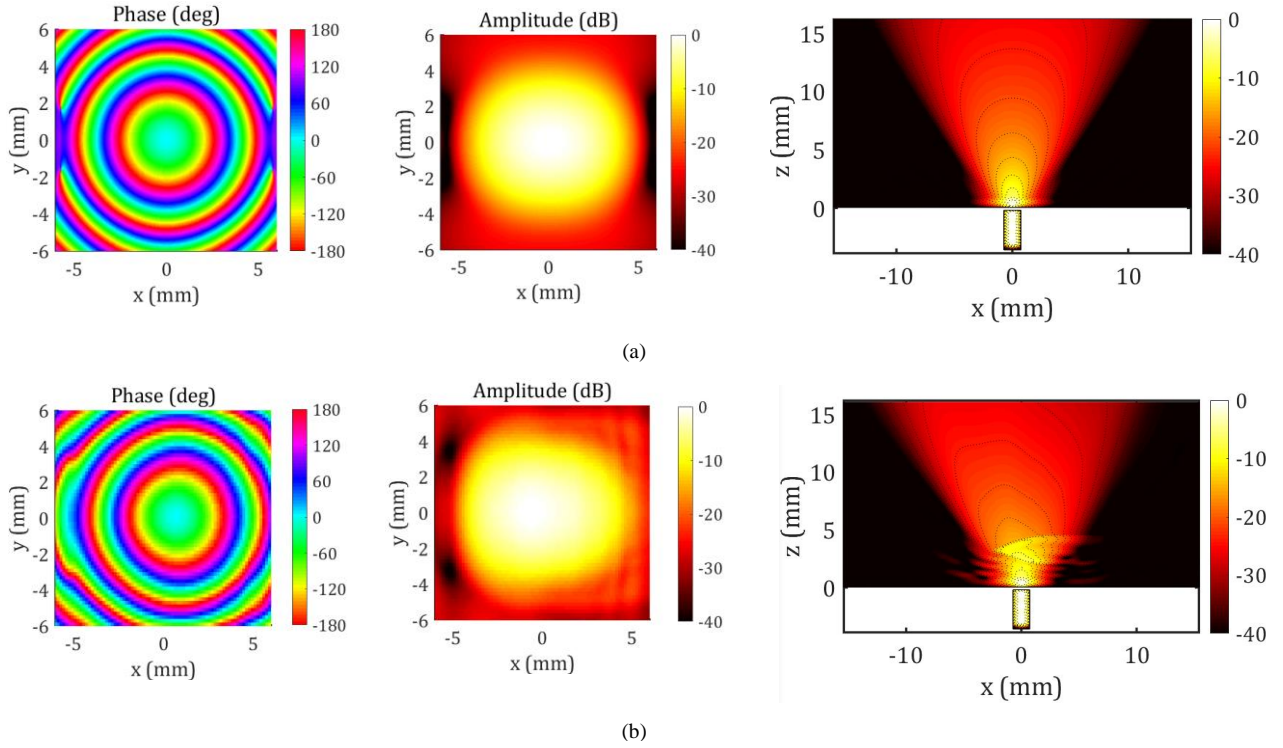
Fig. 9.   Near-field y-component phase and amplitude at S_i and $y = 0$ (Fig. 5b) for a) LW feed without GW b) LW feed with GW.

known $[\vec{E}_a, \vec{H}_a]$ over a plane, and a known incident plane wave angle, the plane where $[\vec{E}_i, \vec{H}_i]$ presents an optimum match with $[\vec{E}_a, \vec{H}_a]$ in terms of phase and amplitude should be found inside the elliptical lens. The vector $\vec{r}_0$ defines the optimum relative position between (x', z') and (x, z) (Fig. 5b) where the LW feed−GW system should be displaced to minimize the scan loss.

Applying the described analysis in reception, $\vec{r}_0$ for the LW feed−GW system has been optimized for the beam steering at $25°$ to minimize the scan loss. This steering angle has been chosen as it represents the scan range limit of the presented concept achieving a reasonable scan loss. The lens diameter ($18\lambda_0 = 30$mm), elliptical lens truncation angle ($40°$), and LW feed geometry correspond to the ones reported in [1]. The resulting optimum displacement is $\vec{r}_0 = \Delta x \hat{x} + \Delta z \hat{z}$, with $\Delta x = 7.3$mm and $\Delta z = 4$mm. Fig. 10 shows the incident field amplitude and phase for a $25°$ incident plane-wave in the plane $z' = 8.7$mm. In this plane, the best field match to the field transmitted after the gratings at S_i (Fig. 9), $z = 4.7$mm in Fig. 5b, is found.

The η_{ap} of the beam pointing at $25°$ for the optimized feed with GW is -4.4dB at 180GHz, estimated with the analysis in reception. The contributions to η_{ap} are: phase efficiency -1dB, spill-over and reflection efficiency -2.6dB, taper and polarization efficiency: -0.7dB. This leads to a scan loss, with respect to the η_{ap} of the broadside beam reported in [1] with the same LW feed, of only -3.6dB. This result represents a significant improvement w.r.t the -7.8dB that one would get by displacing the feed in the focal plane, as in [1]. These good performances were achieved by choosing a good compromise

between field taper at the edge of the grating (as discussed in Section III.A) and phase slope. Indeed, considering the same feed location, optimized for the feed with gratings, the amplitude modification in the LW feed field originated by the gratings (Fig. 9b) enhances the taper efficiency in approx. 1dB, with respect to the amplitude characteristic in the LW feed without gratings (Fig. 9a).

For the sake of comparison, the analysis in reception has been as well applied to optimize $\vec{r}_0$ for $25°$ steering for the LW feed without gratings. The cases where the feed is displaced along the focal plane (Fig. 2a) and where its position has also been optimized axially (Fig. 2c) have been evaluated. Fig. 11a compares the FW simulated radiation patterns at the center frequency for the beams pointing at $25°$ for 1) the LW feed displacing along the focal plane ($\Delta x = 8.9$mm), 2) the LW feed position optimized laterally and axially ($\Delta x = 7.6$mm, $\Delta z = 5$mm) and 3) the LW feed with GW optimized laterally and axially ($\Delta x = 7.3$mm, $\Delta z = 4$mm). Here, the beam symmetry and directivity improvement with the GW can be appreciated. Moreover, 2dB higher aperture efficiency is achieved at the center frequency thanks to the proposed GW.

In Fig. 11b, the scan loss and steering angle over frequency are displayed for the beams steering to $25°$. The results show wideband scan loss improvement. The scan loss is better than -4.1dB in the whole frequency band, with respect to the broadside beam reported in [1]. The improvement w.r.t. the cases without GW is higher than 1.2dB over the whole bandwidth. The steering angle is more stable for the lens with GW over the whole frequency band, due to the lower impact of multiple reflections.
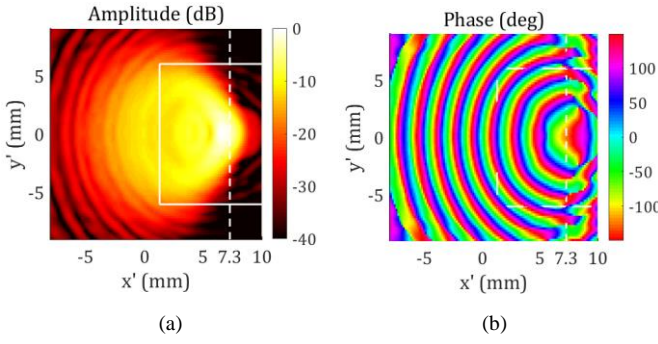
(a)   (b)

Fig. 10. y-component of the incident field $\vec{E}_i$ at $z' = 8.7$mm for a y-polarized plane-wave with 25° oblique incidence, considering an elliptical lens with $\varepsilon_r = 2.3$, $D = 30$mm and truncation angle 40°, at 180GHz. a) Amplitude, b) Phase. Reference system (x', y') as defined in Fig. 5a. For reference, the plane $y = 0$ for the LW feed−GW system has been marked with dashed white lines, and the range where Fig. 9b is shown is plotted with solid white lines.
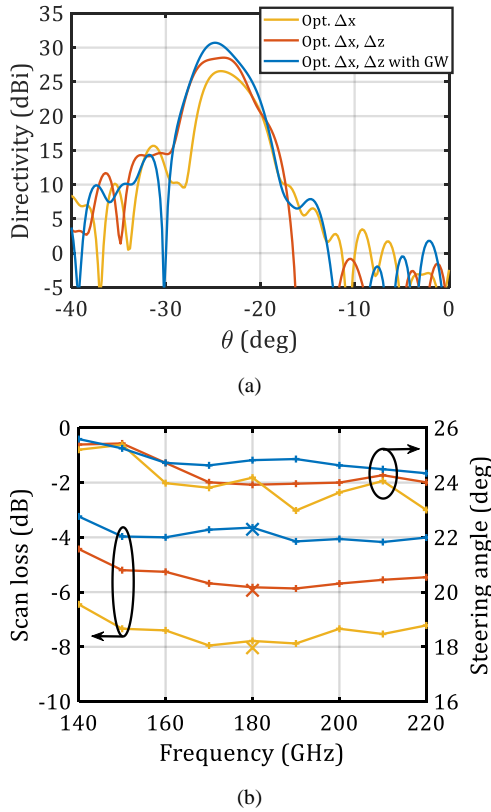

(a)

(b)

Fig. 11. a) FW simulated radiation pattern comparison for beam steering to 25° on the H-plane at 180GHz for 1) the LW feed displacing along the focal plane, 2) the LW feed position optimized laterally and axially and 3) the LW feed with GW optimized laterally and axially. b) FW simulated scan loss (w.r.t. the η_{ap} of the broadside beam reported in [1]) and scan angle over frequency for the beam pointing at 25°, for the three configurations listed in a). Crosses: scan loss calculated with the analysis in reception.

Applying the analysis in reception, $\vec{r}_0$ has been optimized in terms of scan loss for different steering angles. The goal is to cover the whole targeted steering range ($\pm 25°$) with multiple simultaneous beams crossing at -3dB. This would be the objective in a small cell scenario, as described in [33]. For an elliptical lens with 30mm diameter (~ 34dBi directivity at the center frequency), a steering range of $\pm 25°$ can be covered with

15 beams. The LW feed geometry and elliptical lens truncation angle are for all beams the same as in [1].

The scan loss for each beam, calculated with the analysis in reception, is shown in Fig. 12a. The corresponding Δx and Δz values are displayed in Fig. 12b. Only the beams with scan loss higher than 1dB have been provided with a GW (marked with circles in Fig. 12). For the sake of comparison, the results for the LW feed without GW, optimized along the focal plane and also axially, are also shown. Fig. 13 shows the radiation patterns for the beams pointing at 14.4°, 21.6° and 25°, estimated with FW simulations.
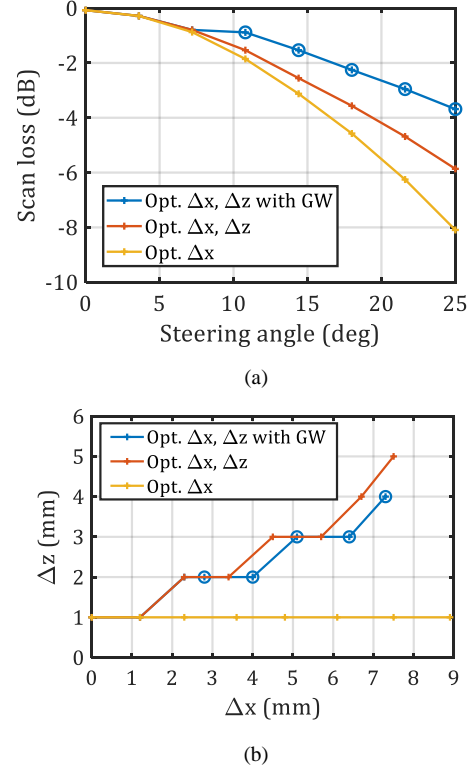

(a)

(b)

Fig. 12. a) Scan loss comparison for elliptical lens steering on the H-plane with 1) the LW feed displacing along the focal plane, 2) the LW feed position optimized laterally and axially and 3) the LW feed with GW optimized laterally and axially. b) Δx and Δz for the beams reported in a). The circles represent the cases where the GW has been used. The scan loss is calculated w.r.t. the broadside beam from [1] (lens without GW), displayed in Fig. 13.

V. PROTOTYPE FABRICATION AND MEASUREMENTS

A prototype has been fabricated in order to validate the performance of the lens with integrated GW, for the beam steering at 25° (Fig. 14). The wave-guide split-block and double-slot shown in [1] are used as well in this prototype. The wave-guide split-block presents several positioning holes where the lens can be fixed w.r.t. the feed for the different beam steering, as shown in [1]. The elliptical lens has been fabricated in HDPE material (High Density Polyethylene, $\varepsilon_r = 2.3$) due to its very low loss properties ($\tan \delta = 3.4 \times 10^{-4}$); the gratings layers have been fabricated in Topas material ($\varepsilon_r = 2.3$, $\tan \delta = 1.2 \times 10^{-3}$), due to the material hardness which enables the fabrication with standard milling [37].
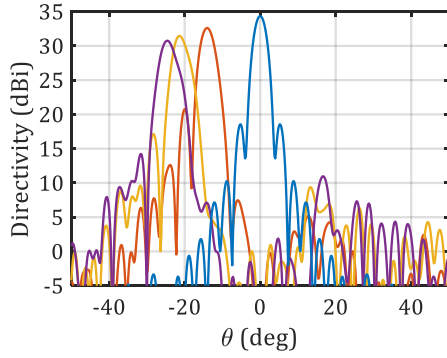
Fig. 13. FW directivity at 180GHz including multiple reflections for the beams pointing at 14.4° (red line), 21.6° (yellow line), and 25° (purple line), all for the lens with GW, simulated with EMPIRE XPU (H-plane). The broadside beam from [1] (without GW) has been included as reference (blue line). The feed Δx and Δz corresponds to the one reported in Fig. 12b (optimized Δx and Δz with GW).

(a)

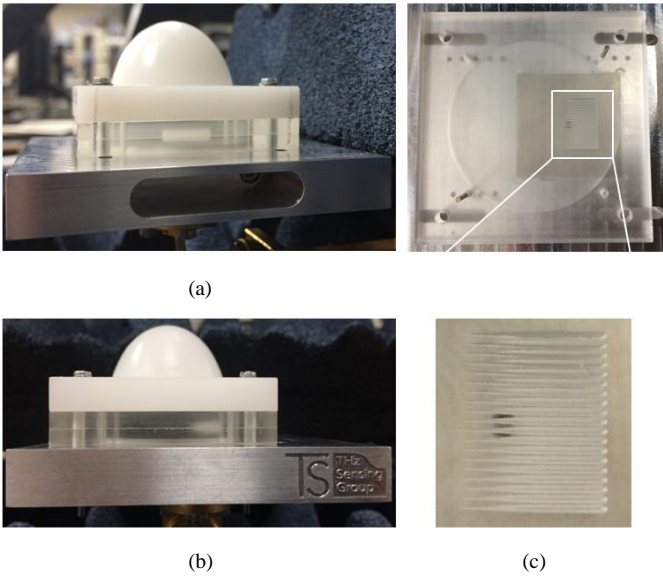(b)   (c)

Fig. 14. a) Prototype side view. b) Prototype front view (see Fig. 1). c) Top view of fabricated dielectric gratings. The feed double-slot on top of the waveguide can be appreciated in black below the Topas layer.

The antenna reflection coefficient has been measured and compared to the reflection coefficient of the lens without GW. The results, displayed Fig. 15, show that the use of the GW does not modify the impedance matching results.

The far-field patterns have been characterized by measuring the near-field on a plane on top of the lens antenna, by means of an open-ended waveguide. The sampling is performed by an automatic positioner, to which the VNA with the open-ended waveguide is fixed. A plane with $50 \times 50\text{mm}^2$ area has been measured, displaced 30mm w.r.t. the ellipse symmetry axis, in order to capture the energy corresponding to the main beam. In Fig. 16, the FW simulated and measured radiation patterns are compared, showing good agreement. Measurement results for a beam steering to 25° in the lens without gratings wedge from [1] are included as well. These measurements have been performed with the feed positioned at $\Delta z = 2.4\text{mm}$ and $\Delta x = 8.4\text{mm}$, due to the location of existing positioning holes. The

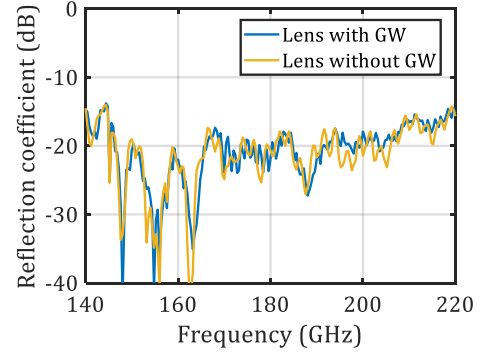resulting radiation patterns feature higher side lobe levels than in the prototype with GW.

Fig. 15. Measured reflection coefficient for the elliptical lens with GW, compared to the measurements without GW from [1].

Fig. 17 shows the maximum gain over frequency for the beams pointing at 25°. Results with and without GW are shown as well here. In order to account for the power lost in spill-over and not captured in the measurement plane, the gain has been normalized by the power radiated by the antenna at broadside in [1]. The gain of this antenna is known, as reported in [1], and therefore its radiated power can serve as a reference. The simulated scan loss, taking into account the lens dielectric loss, is 3.9dB at the center frequency. This differs in 0.3dB w.r.t. the scan loss calculated with the directivity, as the dielectric loss is higher for a beam steering at 25° than at broadside. Measurement results show 4.4dB scan loss at the center frequency, showing a 0.5dB difference w.r.t. FW simulations. This is in accordance with the expected fabrication and measurement tolerances.

Finally, Table I compares the scanning performance of different integrated lens concepts proposed in the literature. The steering range w.r.t. the conventional elliptical lens in [1] is enhanced without increasing the lens aspect ratio, height/D.

VI. CONCLUSION

In this contribution, a new approach to enhance the scan range in low$-\varepsilon_r$ lenses with planar focal plane at sub-THz frequencies is presented. A wedge of dielectric gratings is integrated inside the elliptical lens, reducing the spillover and reflection loss for the off-axis beams. This concept is enabled thanks to the directive patterns of the resonant LW used as lens feed. An analysis in reception is applied to optimize the optimum position of the feed and gratings wedge, minimizing the scan loss.

In this work, we have demonstrated the steering enhancement for the H-plane. In this case, the gratings height varies along each row to maximize the tilt in the feed radiation pattern. The scan loss reached for the beam pointing at 25° is 3.6dB at the center frequency, reaching 30dBi gain. This represents an improvement of 4dB w.r.t. the scan loss for the feed without gratings wedge displaced along the focal plane [1]. The scan loss enhancement is visible over 44% relative bandwidth. A prototype with a beam steering of 25° has been
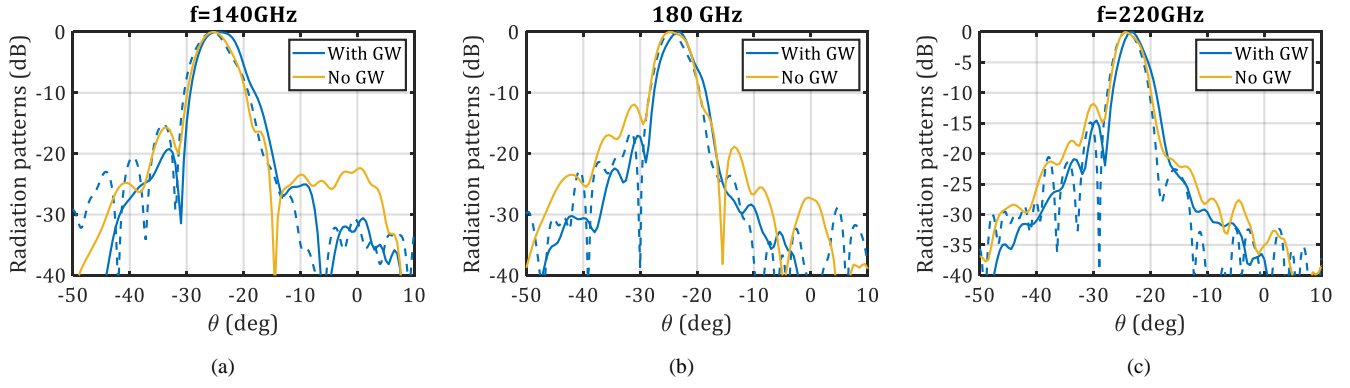
Fig. 16. Measured and FW simulated radiation patterns for the elliptical lens with and without GW, steering to 25°. The beam without GW is measured with the feed at $\Delta z = 2.4$mm and $\Delta x = 8.4$mm. Solid line: measurements. Dashed line: FW simulations. a) 140GHz, b) 180GHz, c) 220GHz.

TABLE I
SIMULATED SCANNING PERFORMANCE OF INTEGRATED LENSES

Ref.	f_0 (GHz)	Lens ε_r	Broadside directivity (dBi)	Broadside gain (dBi)	Gain BW (%)	Impedance BW (%)	Steering range (°)	Broadside η_{ap} (dB)	Scan loss (dB)	SLL (dB)	Antenna height/D
[6]	62.5	5.5 & 2.53	24.9	18.3	40	40	20	−7	< 1	−12	0.78
[7]	77	3.01	31.2	28.7	5	-	30	−2.8	1.1	−15	1.05
[8]	100 / 500	11.7	- / 37	-	-	5	45 / 28	- / −5	4 / 3	−12	0.7 / 0.68
[10]*	27.3	2.7 & 2.05	22	19	15	5	45 / 60	−2.8	2.6 / 5	−12	0.64
[11]	77	3.8	21 / 24.5	-	-	-	25	39 / 27	−0.6 / −1.5	7 / 2	−15	0.86
[1]	180	2.3	34.5	34	44	44	16	−0.4	3.6	−15	1.1
This work	**180**	**2.3**	**34.5**	**34**	**44**	**44**	**25**	**−0.4**	**3.6**	**−15**	**1**

(*) This concept requires an array feeding network.

fabricated and characterized at G-band (140–220GHz), validating FW simulation results and fabrication process. For the E-plane scanning, similar performances are expected. Due to the gratings anisotropy, in this case the height variation in the dielectric gratings should be performed along the period to reach the maximum tilt in the feed pattern. This configuration leads to slightly lower tilt in the feed pattern w.r.t. the H-plane (7% less). This small difference will lead to slightly higher but comparable scan loss performance.
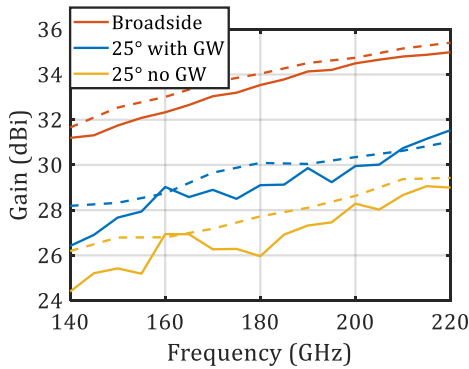

Fig. 17. Measured (solid lines) and FW simulated (dashed lines) maximum gain for the radiation patterns steering to 25° in Fig. 16. The beam without GW is measured with the feed at $\Delta z = 2.4$mm and $\Delta x = 8.4$mm. The measured and FW simulated gain for the broadside beam in [1] is also shown as reference.

APPENDIX I.　SELECTION OF GRATING GEOMETRY

In this appendix, we discuss the choice of the pyramidal grating geometry for the proposed lens antenna. In this work, a linear phase shift is introduced by changing locally the permittivity of the lens using a grating wedge. The proposed grating wedge is used to introduce a beam tilt in the feed, and not to perform pattern collimation as in [17]. The pattern collimation is provided only by the elliptical lens. In this way, lower phase shifts for the grating geometry are required.

A crucial advantage of pyramidal grating geometries is their suitability to be fabricated with standard milling processes at frequencies higher than 100GHz. The grating period needs to be kept small to avoid the appearance of grating lobes. Rectangular [23] or cylindrical gratings [25] with straight walls and small periodicity lead to prohibitive aspect ratios, which are not feasible to be manufactured with standard milling techniques at these high frequencies. Currently, material restrictions, roughness, and tolerances in 3D printing techniques lead to lower accuracies than milling techniques at these high frequencies, to the best of our knowledge. Pyramidal structures with small periods can be manufactured by choosing a milling tool with conical end, matching the pyramid slant angle α [37]. The choice of a 1D structure facilitates the fabrication further w.r.t. 2D geometries.

In Fig. 18, simulation results are displayed for 1D mirrored unit cells with different geometries, embedded in dielectric material. The simulations are performed with the EMT-FqM model (Appendix II). The evaluated parameters are the phase shift Ψ w.r.t. the unit cell filled with dielectric material, (1) (Fig. 18b), and the transmission coefficient (Fig. 18c). The height is

kept constant ($h = h_{max} = 0.76\lambda_d$), and the slant angle α is varied in different configurations (Fig. 18a). The period is kept smaller than 550µm, as larger periods would lead to grating lobes. All results are evaluated for broadside incidence, TE mode, $\phi = 0°$ (Fig. 3b) and at the center frequency (180GHz). In Variation I, a rectangular unit cell with dielectric width $p/2$ is the starting point (effective permittivity $\varepsilon_{eff} \sim 1.44$). α is then incremented, keeping the period $p = 550$µm, as well as a constant dielectric width at $h/2$. In this case, there is almost no impact in the achieved Ψ, but the transmission coefficient is enhanced for larger α. In Variation II, a rectangular unit cell with dielectric width 30µm is the starting point ($\varepsilon_{eff} \sim 1.03$). α is incremented keeping the period $p = 550$µm, as well as a constant dielectric width at h. Ψ decreases in this case for larger α. Finally, in Variation III the fabrication restrictions are considered (see Section II.B), fixing $t_{top} = 30$µm and $t_{bot} = 100$µm. p varies therefore in this case with α ($p = 130, ... , 550$µm, $\varepsilon_{eff} \sim 1.15$ for $\alpha = 0°$). Ψ decreases also here for larger α. As predicted, in general larger phase shifts are reached for smaller α, but at the cost of worsening the transmission coefficients. In our design, larger phase shifts would be desired to reduce further the scan loss. Nevertheless, $\alpha = 9.3°$ is finally chosen, as it is the limit of the minimum slant angle that can be achieved in the tool. This leads in our case to a period of 550µm, sufficient to avoid grating lobes when illuminated with the proposed LW feed.

(a)

(b)
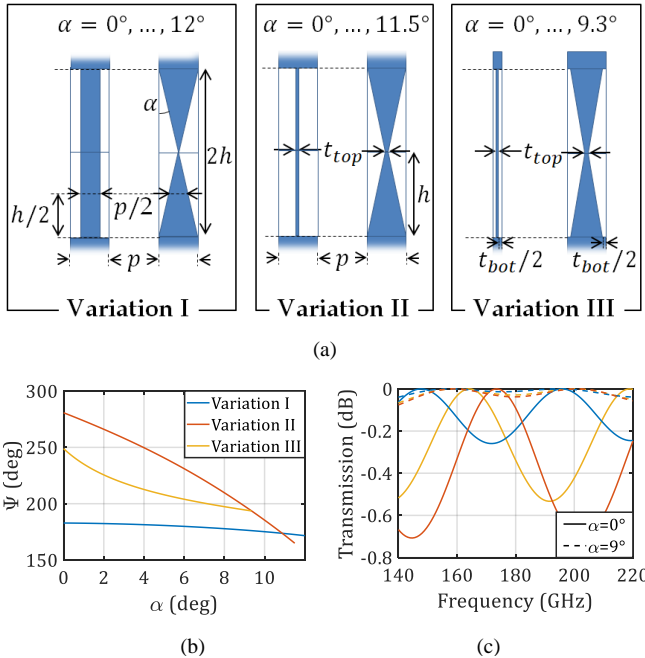
(c)

Fig. 18. a) Variations in the slant angle α. Variation I: fixed $p = 550$µm; fixed dielectric width $p/2$ at $h/2$. Variation II: fixed $p = 550$µm and pyramid top $t_{top} = 30$µm. Variation III: fixed $t_{top} = 30$µm, and tool tip width, $t_{bot} = 100$µm; variable period, $p = 130, ... , 550$µm. b) Phase shift as defined in (1) over α for the variations shown in a). c) Transmission coefficient over frequency for all variations for $\alpha = 0°$ and $9°$. The colors correspond to the legend in b).

APPENDIX II.   DIELECTRIC GRATINGS MODELING

The electromagnetic wave propagation along periodic sub-wavelength dielectric gratings can be modelled as the propagation through equivalent homogeneous media. The EMT derives the electromagnetic properties of the equivalent homogeneous media for a given grating geometry (e.g. effective dielectric permittivity). Closed-form solutions for the EMT effective permittivity of 1D rectangular or lamellar gratings [23], 2D rectangular gratings [24], cylindrical perforations [25] or pyramidal gratings with different bases [26] have been derived in the literature. Besides, 1D gratings can be evaluated more accurately as a stack of multiple thin layers with rectangular lamellar geometry. This was already proposed in [22], [28]–[29] for circular rods, triangular, sinusoidal or arbitrary profiles. In this work, this approach will be followed to calculate the phase of the transmitted wave along the pyramidal gratings. Fig. 19 shows the representation of a grating as a stack of $n = 1:N$ 1D rectangular gratings with height $l \ll h$. Each of them can be approximated as a uniaxial anisotropic medium, where the axes are aligned with the grating symmetry axes. The effective permittivity tensor is defined for the n-th layer as

$$\bar{\bar{\varepsilon}}_n = \begin{pmatrix} \varepsilon_n^\parallel & 0 & 0 \\ 0 & \varepsilon_n^\perp & 0 \\ 0 & 0 & \varepsilon_n^\parallel \end{pmatrix} \quad (8)$$

with the coordinate system in Fig. 19. As the grating period is not extremely small with respect to the wavelength ($0.6\lambda_d$ at the highest frequency), a second-order solution respect to the period-to-wavelength ratio, α, has been considered to calculate the effective permittivity [22]. The expressions for $\varepsilon_n^\parallel$ and $\varepsilon_n^\perp$, depend as well on its the dielectric material fill factor in the n-th layer, $f_n = w_d/w_t$ (Fig. 19), the ε_r in both the dense medium, ε_2, and the medium where the gratings are immerse, ε_1. As reported in [22]

$$\varepsilon_n^\parallel = \varepsilon_n^0 + \frac{\pi^2}{3}[f_n(1-f_n)(\varepsilon_2 - \varepsilon_1)]^2 \alpha^2 \quad (9a)$$

$$\varepsilon_n^\perp = \frac{1}{a_n^0} + \frac{\pi^2}{3}\left[f_n(1-f_n)\frac{\varepsilon_2-\varepsilon_1}{\varepsilon_2\varepsilon_1}\right]^2 \frac{\varepsilon_n^0}{(a_n^0)^3}\alpha^2 \quad (9b)$$

where $\varepsilon_n^0 = \varepsilon_2 f_n + \varepsilon_1(1-f_n)$ and $a_n^0 = f_n/\varepsilon_2 + (1-f_n)/\varepsilon_1$. In our design, $\varepsilon_1 = 1$ and $\varepsilon_2 = 2.3$. This model assumes that only the fundamental mode is supported in the gratings layer, and therefore the grating depth does not appear as a variable [30]. The dependency of the effective permittivity with respect to the angle of incidence [27], [31] has been as well neglected. The error introduced by these assumptions will be later on quantified comparing the EMT model with FW Floquet mode simulations.

In order to evaluate the reflection and transmission properties of the stack of thin uniaxial anisotropic media, methods such as the thin-film theory [28] or linearization of Ricatti differential equation for small reflections [29] have been proposed in the literature. In this work, we propose to apply an equivalent transmission line (TL) model [39] with N-sections in z of thickness l. In this way, we account for all multiple reflections in the pyramidal structure. The TL model is applied in the two principal planes, aligned with the anisotropy axis (planes $\phi = 0°$ and $\phi = 90°$ in Fig. 19). In these planes the transmitted field for an incident plane-wave can be described as well as a single plane-wave [40], and TE and TM modes are de-coupled. The

propagation constants and characteristic impedances for the TE and TM equivalent transmission lines have been estimated from the theory of wave propagation in anisotropic multi-layer media at oblique incidence [41].
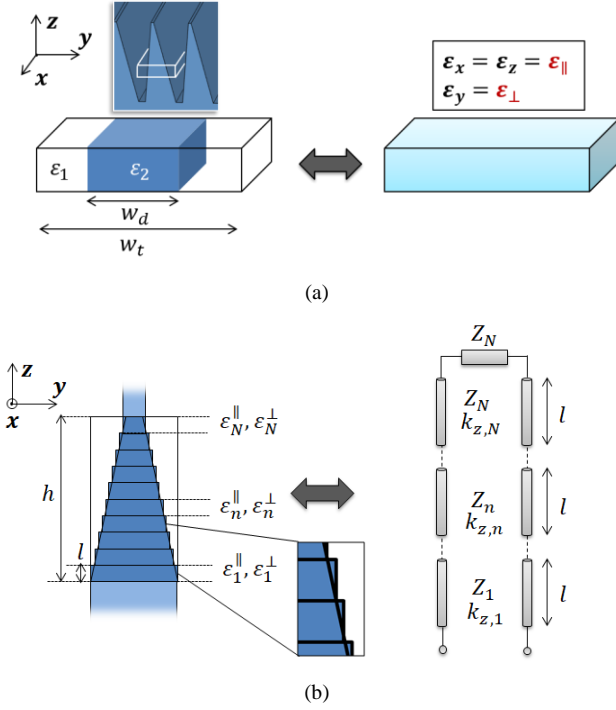

(a)

(b)

Fig. 19. a) Dielectric squared grating and its equivalent homogeneous anisotropic medium. b) Pyramid-pair discretization and equivalent transmission line model.

For each layer in the stack, the propagation in the $\phi = 0°$ plane can be described considering different effective permittivity for the TM and TE modes, as $\varepsilon_n^{TM} = \varepsilon_n^{\parallel}$ and $\varepsilon_n^{TE} = \varepsilon_n^{\perp}$. As $\varepsilon_n^x = \varepsilon_n^z = \varepsilon_n^{\parallel}$, the effective permittivity for the TM mode is independent from the incident angle. The propagation constant in a n-th section of the TL is then calculated as reported in [39]

$$k_{z,n}^{TM/TE} = \sqrt{\varepsilon_n^{TM/TE} k_0^2 - k_\rho^2} \qquad (10)$$

where $k_\rho = k_0\sqrt{\varepsilon_2}\sin\theta$, being θ the wave vector direction in the host dielectric. The impedances for the TE and TM modes in $\phi = 0°$ are defined for this section as reported in [39]

$$Z_n^{TM} = \frac{\zeta_0}{\sqrt{\varepsilon_n^{TM}}}\frac{k_{z,n}^{TM}}{k_n^{TM}} \qquad (11a)$$

$$Z_n^{TE} = \frac{\zeta_0}{\sqrt{\varepsilon_n^{TE}}}\frac{k_n^{TE}}{k_{z,n}^{TE}} \qquad (11b)$$

where $k_n^{TM/TE} = \sqrt{\varepsilon_n^{TM/TE}}k_0$, and ζ_0 is the wave impedance in vacuum. In the plane $\phi = 90°$, $k_{z,n}^{TE}$ and Z_n^{TE} can be defined as above, this time with $\varepsilon_n^{TE} = \varepsilon_n^{\parallel}$. However, for the TM mode, as $\varepsilon_n^y = \varepsilon_n^{\perp} \neq \varepsilon_n^z$, ε_n^{TM} is dependent on the wave vector direction in the evaluated n-th layer, θ_n, as reported in [41]

$$\varepsilon_n^{TM} = \frac{\varepsilon_n^{\perp}\varepsilon_n^{\parallel}}{\varepsilon_n^{\perp}\sin^2\theta_n + \varepsilon_n^{\parallel}\cos^2\theta_n} \qquad (12)$$

where θ_n is calculated with the Snell's Law for multilayer anisotropic media, as reported in [41]

$$\sin\theta_n = \frac{\sqrt{\varepsilon_{n-1}^{\perp}\varepsilon_{n-1}^{\parallel}\varepsilon_n^{\parallel}}\sin\theta_{n-1}}{\sqrt{\varepsilon_n^{\perp}\varepsilon_n^{\parallel}(\varepsilon_{n-1}^{\perp}-\varepsilon_{n-1}^{\parallel})-\varepsilon_{n-1}^{\perp}\varepsilon_{n-1}^{\parallel}(\varepsilon_n^{\perp}-\varepsilon_n^{\parallel})\sin^2\theta_{n-1}+\varepsilon_n^{\perp}\varepsilon_n^{\parallel}\varepsilon_{n-1}^{\parallel}}} \qquad (13)$$

where $\varepsilon_{n-1}^{\perp}$ and $\varepsilon_{n-1}^{\parallel}$ are the yy and zz tensor components and θ_{n-1} the incident angle in the medium where the incident wave propagates. $k_{z,n}^{TM}$ is calculated with ε_n^{TM} from (12) in the same way as in the $\phi = 0°$ plane. Instead, the equation for the calculation of Z_n^{TM} becomes for $\phi = 90°$, as reported in [41]

$$Z_n^{TM} = \frac{\zeta_0\sqrt{\varepsilon_n^{TM}}}{\varepsilon_n^{\perp}}\frac{k_{z,n}^{TM}}{k_n^{TM}} \qquad (14)$$

Once the propagation constants and characteristic impedances have been calculated for each layer, the computation of the transmission matrix (ABCD) for the full stack is calculated with a standard concatenation of ABCD matrices as

$$\begin{bmatrix} A_T & B_T \\ C_T & D_T \end{bmatrix} = \Pi_1^N \begin{bmatrix} A_n & B_n \\ C_n & D_n \end{bmatrix} \qquad (15)$$

where $A_n = \cos(k_{z,n}^{TE/TM}l)$, $B_n = jZ_n^{TE/TM}\sin(k_{z,n}^{TE/TM}l)$, $C_n = (j/Z_n^{TE/TM})\sin(k_{z,n}^{TE/TM}l)$ and $D_n = A_n$ [42].

The Scattering Parameters (S-parameters) are calculated from the resulting ABCD matrix. For a single pyramid, the reference impedance for the S-parameter calculation is the one in the dielectric for the pyramid base side, and the one of the last slab in the pyramid tip. These would be the boundary conditions when using mirrored pyramids. For two mirrored pyramids, the reference impedance is the one in the dielectric on both sides, as they will be embedded in the elliptical lens dielectric.

The transmission line model has been validated with FW Floquet mode simulations in CST Studio Suite [43] for a unit cell with periodic boundary conditions. S-parameter results for a pyramid-pair for broadside and oblique incidence are shown in Fig. 20. The validation is shown for gratings with $h_{max} = 1.27$mm. The discrepancies of the model w.r.t. FW simulations are related to the large period in the considered structure ($0.6\lambda_d$ at the highest frequency). This compromises the accuracy of the EMT method applied [22]. The results show therefore a better match in the low part of the frequency band, where the period is smaller in terms of wavelength. Nevertheless, the accuracy reached in the analytic results is sufficient for the application discussed in this paper.
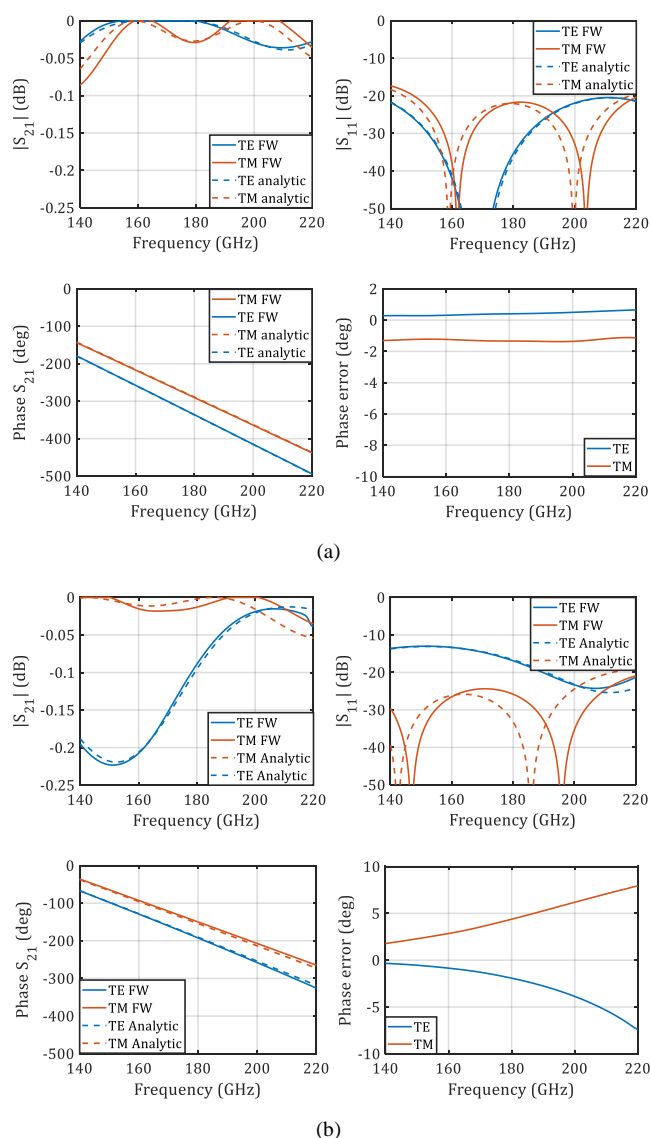
ACKNOWLEDGMENT

(a)

(b)

Fig. 20. Transmission coefficients for two mirrored dielectric pyramids with height 1275μm a) Broadside incidence b) Obliquus incidence for $\phi = 90°$, $\theta = 30°$. The phase error refers to the difference between FW and analytic results for the S_{21} phase.

REFERENCES

[1] M. Arias Campo, D. Blanco, S. Bruni, A. Neto, and N. Llombart "On the use of Fly's eye lenses with leaky wave feeds for wideband wireless communications," *IEEE Trans. Antennas Propag.*, vol. 68, no. 4, pp. 2480–2493, Apr. 2020.

[2] M. Arias Campo, G. Carluccio, D. Blanco, O. Litschke, S. Bruni, and N. Llombart, "Wideband circularly polarized antenna with in-lens polarizer for high-speed communications", *IEEE Trans. Antennas Propag.*, vol. 69, no. 1, pp. 43–54, Jan. 2021.

[3] H. Chou, Y. Chang, H. Huang, Z. Yan, T. Lertwiriyaprapa and D. Torrungrueng, "Optimization of Three-Dimensional Multi-Shell Dielectric Lens Antennas to Radiate Multiple Shaped Beams for Cellular Radio Coverage," in *IEEE Access*, vol. 7, pp. 182974–182982, 2019.

[4] C. Wang, Y. Xia, G. Guo, M. Nasir and Q. Zhu, "Ellipsoidal Luneburg Lens Binary Array for Wide-Angle Scanning," in *IEEE Transactions on Antennas and Propagation*, vol. 68, no. 7, pp. 5702–5707, July 2020.

[5] H. F. Ma, B. G. Cai, T. X. Zhang, Y. Yang, W. X. Jiang and T. J. Cui, "Three-Dimensional Gradient-Index Materials and Their Applications in Microwave Lens Antennas," in *IEEE Transactions on Antennas and Propagation*, vol. 61, no. 5, pp. 2561–2569, May 2013.

[6] J. R. Costa, M. G. Silveirinha, and C. A. Fernandes, "Evaluation of a double-shell integrated scanning lens antenna," *IEEE Antennas And Wireless Prop. Letters,* vol. 7, pp. 781–784, Oct. 2008.

[7] N. T. Nguyen, A. V. Boriskin, L. Le Coq, and R. Sauleau, "Improvement of the scanning performance of the extended hemispherical integrated lens antenna using a double lens focusing system," *IEEE Trans. Antennas Propag.*, vol. 64, no. 8, pp. 3698–3702, Aug. 2016.

[8] G. C. Trichopoulos, G. Mumcu, K. Sertel, and H. Lee Mosbacker, "A novel approach for improving off-axis pixel performance of terahertz Focal Plane Arrays," *IEEE Trans. Microw. Theory and Techn.*, vol. 58, no. 7, pp. 2014–2021, July 2010.

[9] A. V. Boriskin and R. Sauleau, "Numerical investigation into the design of shaped dielectric lens antennas with improved angular characteristics," *Prog. Electromagn. Res. B*, vol. 30, pp. 279–292, May 2011.

[10] K. Liu, S. Yang, S. Qu, C. Chen, and Y. Chen, "Phased Hemispherical Lens Antenna for 1-D Wide-Angle Beam Scanning," in *IEEE Transactions on Antennas and Propagation*, vol. 67, no. 12, pp. 7617–7621, Dec. 2019.

[11] A. Artemenko, A. Mozharovskiy, A. Maltsev, R. Maslennikov, A. Sevastyanov, and V. Ssorin, "Experimental characterization of E-band two-dimensional electronically beam-steerable integrated lens antennas," *IEEE Antennas and Wireless Prop. Letters*, vol. 12, pp. 1188–1191, Oct. 2013.

[12] J. Gonzalez Marin and J. Hesselbarth, "Lens antenna with planar focal surface for wide-angle beam-steering application," *IEEE Trans. Antennas Propag.*, vol. 67, no. 4, pp. 2757–2762, Apr. 2019.

[13] E. Tolin, O. Litschke, S. Bruni and F. Vipiana, "Compact Extended Scan Range Antenna Array Based on Rotman Lens," in *IEEE Transactions on Antennas and Propagation*, vol. 67, no. 12, pp. 7356–7367, Dec. 2019.

[14] M. Mencagli, Jr. *et al*, "Beam squinting metalens design and its application to multibeam reflector feeds," *in Proc. 11ᵗʰ European Conference on Antennas and Propagation (EuCAP)*, Paris, France, Mar. 2017.

[15] M. Imbert, A. Papió, F. De Flaviis, L. Jofre and J. Romeu, "Design and Performance Evaluation of a Dielectric Flat Lens Antenna for Millimeter-Wave Applications," *in IEEE Antennas and Wireless Propagation Letters*, vol. 14, pp. 342–345, 2015.

[16] M. Akbari, M. Farahani, A. Ghayekhloo, S. Zarbakhsh, A. Sebak and T. A. Denidni, "Beam Tilting Approaches Based on Phase Gradient Surface for mmWave Antennas," *in IEEE Transactions on Antennas and Propagation*, vol. 68, no. 6, pp. 4372–4385, June 2020.

[17] F. Maggiorelli, A. Paraskevopoulos, J. Vardaxoglou, M. Albani and S. Maci, "Profile Inversion and Closed Form Formulation of Compact GRIN Lenses," in *IEEE Open Journal of Antennas and Propagation,* vol. 2, pp. 315–325, 2021.

[18] M. K. T. Al-Nuaimi and W. Hong, "Discrete Dielectric Reflectarray and Lens for E-Band With Different Feed," *in IEEE Antennas and Wireless Propagation Letters*, vol. 13, pp. 947–950, 2014.

[19] K.X. Wang and H. Wong, "Design of a wideband circularly polarized millimeter wave antenna with an extended hemispherical lens," *IEEE Trans. Antennas Propag.*, vol. 66, no. 8, pp. 4303–4308, Aug. 2018.

[20] H. Yi, S. Qu, K. Ng, C. H. Chan and X. Bai, "3-D Printed Millimeter-Wave and Terahertz Lenses with Fixed and Frequency Scanned Beam," *in IEEE Transactions on Antennas and Propagation*, vol. 64, no. 2, pp. 442–449, Feb. 2016.

[21] N. T. Nguyen, N. Delhote, M. Ettorre, D. Baillargeat, L. Le Coq and R. Sauleau, "Design and Characterization of 60-GHz Integrated Lens Antennas Fabricated Through Ceramic Stereolithography," *in IEEE Transactions on Antennas and Propagation*, vol. 58, no. 8, pp. 2757–2762, Aug. 2010.

[22] P. Lalanne, "Effective medium theory applied to photonic crystals composed of cubic or square cylinders" *Applied Optics*, Vol. 35, No. 27, Sept. 1996.

[23] S. M. Rytov, "Electromagnetic properties of a finely stratified medium," *Sov. Phys. JETP 2*, pp. 466–475, 1956.

[24] E. B. Grann, M. G. Moharam, and D. A. Pommet, "Artificial uniaxial and biaxial dielectrics with use of two-dimensional subwavelength binary gratings," *J. Opt. Soc. Am.*, vol. 11, no. 10, pp. 2695–2103, Oct. 1994.

[25] M. Mrnka and Z. Raida, "An Effective Permittivity Tensor of Cylindrically Perforated Dielectrics," *in IEEE Antennas and Wireless Propag. Letters*, vol. 17, no. 1, pp. 66–69, Jan. 2018.

[26] A. Deinega, I. Valuev, B. Potapkin, and Y. Lozovik, "Minimizing light reflection from dielectric textured surfaces", *J. Opt. Soc. Am.*, vol. 28, no. 5, pp. 770–777, May 2011.

[27] P. Lalanne and J. P. Hugonin, "High-order effective-medium theory of subwavelength gratings in clasical mounting: application to volume holograms," *J. Opt. Soc. Am.*, vol. 15, no. 7, pp. 1843–1851, Jul. 1998.

[28] X. Jing, J. Ma, S. Liu, Y. Jin, H. He, J. Shao, and Z. Fan, "Analysis and design of transmittance for an antireflective surface microstructure," *Optics Express*, vol. 17, no. 18, pp. 16119–16134, Aug. 2009.

[29] D. H. Raguin and G. M. Morris, "Analysis of antireflection-structured surfaces with continuous one-dimensional surface profiles," *Applied Optics*, vol. 32, no. 4, pp. 2582–2598, May 1993.

[30] Ph. Lalanne and D. Lemercier-Lalanne, ''Depth dependence of the effective properties of subwavelength gratings,'' *J. Opt. Soc. Am.* A 14, 450–458 (1997).

[31] C. W. Haggans and L. Li, "Effective-medium theory of zeroth-order lamellar gratings in conical mountings," *J. Opt. Soc. Am.*, vol. 10, no. 10, pp. 2217–2225, Oct. 1993.

[32] H. Zhang, S. O. Dabironezare, G. Carluccio, A. Neto, and N. Llombart, "A Fourier Optics tool to derive the plane wave spectrum of quasi-optical systems [EM Programmer's Notebook]," *IEEE Antennas and Propag. Magazine*, vol. 63, no. 1, pp. 103–116, Feb. 2021.

[33] N. Llombart, D. Emer, M. Arias Campo, and E. McCune, "Fly's eye spherical antenna system for future Tbps wireless communications," in *Proc. Eur. Conf. Antennas Propag. (EuCAP)*, Paris, France, Apr. 2017.

[34] D. Filipovic, G. Gauthier, S. Raman, and G. Rebeiz, "Off-axis properties of silicon and quartz dielectric lens antennas," *IEEE Trans. Antennas Propag.*, vol. 45, no. 5, pp. 760–766, May 1997.

[35] N. Llombart, G. Chattopadhyay, A. Skalare, and I. Mehdi, "Novel terahertz antenna based on a silicon lens fed by a leaky wave enhanced waveguide," *IEEE Trans. Antennas Propag.*, vol. 59, no. 6, pp. 2160–2168, June 2011.

[36] M. Born and E. Wolf, *Principles of Optics*, 6th edition, 225–226, Pergamon, 1980.

[37] M. Arias Campo, G. Carluccio, D. Blanco, S. Bruni, O. Litschke, and N. Llombart, "Dielectric-grating in-lens polarizer for beyond 5G communications," *in Proc. 44th Int. Conf. on Infrared, Millim. and THz Waves (IRMMW-THz)*, Paris, France, Sept. 2019.

[38] EMPIRE XPU, Available "http://www.empire.de".

[39] L. B. Felsen, M. Mongiardo, and P. Russer, *Electromagnetic field computation by network methods*, Springer Science & Business Media, 2009.

[40] G. Tyras, *Radiation and propagation of electromagnetic waves,* 45–47, Academic Press, 1969.

[41] S. J. Orfanidis, *Electromagnetic Waves and Antennas*, 140–146, 346–350, Rutgers University, 1999.

[42] D. M. Pozar, *Microwave Engineering*, 2nd edition, 196–211, John Wiley & Sons, New York, USA, 1998.

[43] CST Studio Suite, Available "https://www.3ds.com/products-services/simulia/products/cst-studio-suite".